

# Learning Li-ion battery health and degradation modes from data with aging-aware circuit models

Zihao Zhou \*, Antti Aitio, David Howey \*\*

\* *Engineering Science Department, University of Oxford, United Kingdom (e-mail: zihao.zhou@eng.ox.ac.uk).*

\*\* *Engineering Science Department, University of Oxford, United Kingdom (e-mail: david.howey@eng.ox.ac.uk).*

---

**Abstract:** Non-invasive estimation of Li-ion battery state-of-health from operational data is valuable for battery applications, but remains challenging. Pure model-based methods may suffer from inaccuracy and long-term instability of parameter estimates, whereas pure data-driven methods rely heavily on training data quality and quantity, causing lack of generality when extrapolating to unseen cases. We apply an aging-aware equivalent circuit model for health estimation, combining the flexibility of data-driven techniques within a model-based approach. A simplified electrical model with voltage source and resistor incorporates Gaussian process regression to learn capacity fade over time and also the dependence of resistance on operating conditions and time. The approach was validated against two datasets and shown to give accurate performance with less than 1% relative root mean square error (RMSE) in capacity and less than 2% mean absolute percentage error (MAPE). Critically, we show that the open circuit voltage versus state-of-charge function must be accurately known, and any inaccuracies or changes in this over time strongly influence the inferred resistance. However, this feature (or bug) may also be used to estimate *in operando* differential voltage curves from operational data.

*Keywords:* battery, health, estimation, Gaussian process, state space, equivalent circuit, model

---

## 1. INTRODUCTION

Lithium-ion batteries play an important role in the transition to clean energy. Demand is increasing rapidly for grid storage, electric vehicle and home energy storage applications (Tsiropoulos et al., 2018). One of the most crucial challenges for batteries is estimating their state of health (SOH). Accurate estimation of SOH improves lifetime, system safety, and costs of warranties and maintenance. Many studies (Hua et al., 2021; Shahjalal et al., 2022; Zhou et al., 2020) also discuss the importance of dealing with retired batteries, the number of which will increase drastically in the near future. Estimating the evolution of SOH from historical usage data is crucial for enabling possible ‘second-life’ applications that rely on accurate knowledge of battery residual value.

A commonly used SOH indicator, discharge capacity, normally requires the battery to undergo a low-rate constant-current discharge from 100% to 0% state of charge (SOC). This is time consuming, and therefore often not undertaken in real-world applications. Therefore, extensive studies have been done on faster capacity estimation methods (Bericibar et al., 2016; Wang et al., 2020). These are usually categorised into model-driven and data-driven approaches. Model-driven methods use a specific battery model, such as an electrochemical model or electrical equivalent circuit model (ECM), and update the parameters by repeated fitting as the battery ages (Plett, 2004; Gao et al., 2021). Electrochemical models usually need

half-cell test data for parameterization and tend to suffer from parameter identifiability problems (Lu et al., 2021; Miguel et al., 2021). Equivalent-circuit models, the focus in this paper, have fewer parameters but are less connected to physical processes. Recursive state estimation techniques, such as extended Kalman filters (Wassiliadis et al., 2018) and particle filters (Wei et al., 2017), are often adopted for co-estimation of model states and parameters.

On the other hand, data-driven methods for capacity estimation try to map from carefully selected features to corresponding capacity values (Li et al., 2019). Several features indicative of battery usage and aging may be extracted from cell voltage, current, and temperature measurements (Severson et al., 2019; Greenbank and Howey, 2021; Li et al., 2024). Then, machine learning models such as support vector machines (Feng et al., 2019), random forests (Li et al., 2018), neural networks (Li et al., 2021), and Gaussian processes (Richardson et al., 2018), have been used to capture the relationship between these features and capacity. Depending on the choice of inputs, data-driven models can be used either for estimating present SOH, or predicting the future SOH. If the learnt mapping is between input features and future capacity values, these models can be directly used for forecasting. The performance of machine learning models for battery health is largely determined by the breadth, quantity and accuracy of the data used for model training.

Moreover, capacity fade only represents one aspect of battery degradation—increasing impedance (often just represented by resistance) also plays an essential role in battery health (Fu et al., 2021), leading to power fade, which is often correlated with capacity fade. Impedance values may be easier to estimate from cycling data and field data, where capacity measurements are very challenging (Pozzato et al., 2023; Sulzer et al., 2021). Many SOH estimation works treat impedance as a scalar or rely on a look-up table that needs to be calibrated in standard reference tests (Plett, 2004; Locorotondo et al., 2021). However, many experimental works show that impedance does change with operating conditions (Waag et al., 2013; Schönleber et al., 2017).

In this work, we use an aging-aware electrical equivalent circuit model to estimate both capacity and operando battery impedance (resistance) from cycling data. The model parameters are described as functions of aging time and operating conditions (SOC and applied current in this case) and these functions are learned from data using Gaussian process regression. The model builds on former work (Aitio et al., 2023) but with a simpler ECM emphasizing the importance of the estimated resistance. Results show that the learned resistance function is strongly impacted by the assumptions about the battery open circuit voltage (OCV) versus SOC function. This leads to a method to estimate differential voltage ( $dV/dQ$ ) curves indirectly from impedance data. Differential voltage analysis enables deeper understanding of battery aging by quantifying metrics such as loss of lithium inventory (LLI) and loss of active material in each electrode (LAM<sub>n</sub>, LAM<sub>p</sub>) (Dubarry et al., 2012; Dubarry and Anseán, 2022).

Open-source datasets from two batteries (Li et al., 2024; Jöst et al., 2021) with different cycling conditions were used to validate model performance. Our method not only gives accurate estimation for capacity and impedance, but also enables a deeper analysis of battery degradation.

## 2. METHODOLOGY

### 2.1 State space formulation of Gaussian processes

In this work Gaussian processes (GPs) are used to fit functions to data. Full details of GPs are documented in several books and papers, for example Williams and Rasmussen Williams and Rasmussen (2006)—we give only a brief introduction here. A Gaussian process (GP) is defined as a distribution of functions over input  $\mathbf{x}$ , characterised by a mean and covariance, with the covariance defined by a kernel function  $k(\mathbf{x}, \mathbf{x}')$ ,

$$f(\mathbf{x}) \sim \mathcal{GP}(m(\mathbf{x}), k(\mathbf{x}, \mathbf{x}')). \quad (1)$$

When this input includes both locations in space and time  $\mathbf{x} = (s, t)$ , it is often called a spatial-temporal Gaussian process Solin et al. (2016),

$$f(s, t) \sim \mathcal{GP}(m(s, t), k((s, t), (s', t'))). \quad (2)$$

Without loss of generality, the prior mean function  $m(\mathbf{x})$  may be set to zero. By assuming a measurement noise term  $\epsilon$ , the mapping between  $\mathbf{x}$  and  $\mathbf{y}$  can be expressed as

$$\mathbf{y} = f(\mathbf{x}) + \epsilon, \epsilon \sim \mathcal{N}(0, \sigma_n^2 \mathbf{I}). \quad (3)$$

To make predictions, we require the posterior predictive distribution at test samples  $\mathbf{X}^*$  based on observations

from a labeled training set of input-output data  $\mathcal{D} = \{(\mathbf{x}_i, y_i)\}_{i=1}^N$ . In this case, the analytical solution is given by (Williams and Rasmussen, 2006),

$$p(\mathbf{y}^* | \mathbf{X}^*, \mathbf{X}, \mathbf{y}) = \mathcal{N}(\mathbf{y}^* | \mathbf{m}^*, \Sigma^*), \quad (4)$$

where

$$\begin{aligned} \mathbf{m}^* &= \mathbf{K}_{X^*,*}^T [\mathbf{K}_X + \sigma_n^2 \mathbf{I}]^{-1} \mathbf{y} \\ \Sigma^* &= \mathbf{K}_{*,*} - \mathbf{K}_{X^*,*}^T [\mathbf{K}_X + \sigma_n^2 \mathbf{I}]^{-1} \mathbf{K}_{X^*,*}, \end{aligned} \quad (5)$$

and the kernel matrices are simplified as  $\mathbf{K}_X = k(\mathbf{X}, \mathbf{X})$ ,  $\mathbf{K}_{X^*,*} = k(\mathbf{X}, \mathbf{X}^*)$ . For a zero-mean GP, the model is defined by its training data and the selected kernel function  $k(\mathbf{x}, \mathbf{x}')$  including fitted hyperparameters. The negative log maximum likelihood (NLML) estimates of kernel hyperparameters  $\theta$  are given by

$$\begin{aligned} \text{NLML} &= -\log p(\mathbf{y} | \mathbf{X}, \theta) = \\ &= -\frac{1}{2} \mathbf{y}^T [\mathbf{K}_X + \sigma_n^2 \mathbf{I}]^{-1} \mathbf{y} - \frac{1}{2} \log |\mathbf{K}_X| - \frac{n}{2} \log 2\pi. \end{aligned} \quad (6)$$

Large datasets pose challenges for GPs due to the requirement for inversion of an  $N \times N$  matrix (equations 5 and 6) which scales computationally at  $\mathcal{O}(n^3)$ . To address this, we adopt a state-space formulation of a GP that instead scales linearly with the ‘time’ dimension,  $\mathcal{O}(n)$ .

Proposed by Särkkä et al. (Sarkka et al., 2013) and Solin (Solin et al., 2016), the state-space formulation interprets a spatial-temporal Gaussian process  $f(s, t)$  as the solution to a linear time-invariant stochastic partial differential equation (LTI-SPDE),

$$\begin{aligned} \frac{\partial \mathbf{x}(s, t)}{\partial t} &= \mathcal{F} \mathbf{x}(s, t) + \mathbf{L} \omega(s, t) \\ \mathbf{y}_t &= \mathcal{H}_t \mathbf{x}(s, t) + \epsilon_t, \quad \epsilon \sim \mathcal{N}(0, \sigma_n^2). \end{aligned} \quad (7)$$

We can evaluate this system of equations over a finite collection of spatial points of interest  $\{s_i\}_1^{n_s}$ . This results in  $n_s$  sets of state vectors,  $(\mathbf{x}(s_1, t), \mathbf{x}(s_2, t), \dots, \mathbf{x}(s_{n_s}, t))$ , where each is

$$\mathbf{x}(s_i, t) = \left[ f(s_i, t), \frac{df(s_i, t)}{dt}, \dots, \frac{df(s_i, t)^{p-1}}{dt^{p-1}} \right]^T. \quad (8)$$

Here,  $\mathcal{F}$  and  $\mathcal{H}$  are linear operators,  $\mathbf{L}$  is a dispersion matrix, and  $\omega(\mathbf{x}, t)$  is a spatially resolved white noise process decided by the spatial kernel. The mathematical foundation comes from the Wiener-Khinchin theorem (Cohen, 1998), which indicates that the GP kernel covariance matrix and the spectral density of a solution process from a LTI-SPDE form a Fourier-transform pair. At a specific spatial point  $s_i$ , all of the time gradient information up to order  $p - 1$  is maintained and propagated into future, and this propagation occurs for all  $n_s$  spatial points. The exact value for  $p$  is decided by the selected time kernel. Intuitively, one can view this approach as constructing a LTI system which takes a white noise process as input and generates an output that is the desired Gaussian process.

To further simplify the problem, we assume kernel separability,

$$k((s, t), (s', t')) = k(s, s') k(t, t'). \quad (9)$$

Under this assumption,  $\mathcal{F}$  and  $\mathcal{H}$  become constant matrices  $\mathbf{F}$  and  $\mathbf{H}$ . As a result, a GP kernel function may be directly mapped to  $\mathbf{F}$ ,  $\mathbf{H}$  and  $\omega(s, t)$ , defining a corresponding LTI system. The practical implementation of eqn. 7 requires it to have a discretized form,

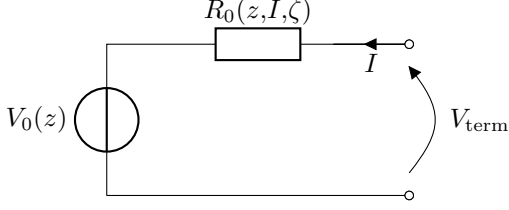


Fig. 1. Equivalent circuit model for Li-ion battery

$$\begin{aligned} \mathbf{x}_k &= \mathbf{A}_{k-1} \mathbf{x}_{k-1} + \mathbf{w}_{k-1} \\ y_k &= \mathbf{H}_k \mathbf{x}_k + v_k, \quad v_k \sim \mathcal{N}(0, \sigma_n^2), \end{aligned} \quad (10)$$

where  $\mathbf{x}_k = [\mathbf{x}_{s_1, k}, \mathbf{x}_{s_2, k}, \dots, \mathbf{x}_{s_{n_s}, k}]^\top$  represents a state vector along all  $n_s$  space locations at time step  $t_k$ , and  $\mathbf{A}_k = \exp(\Delta t_k \mathbf{I}_{n_s} \otimes \mathbf{F})$  is a matrix exponential on  $\mathbf{F}$  and time interval  $\Delta t_k = t_{k+1} - t_k$ . The Kronecker product here comes from the space discretization. Each space location is propagated in time individually, and correlations in space are captured by the process noise term  $\mathbf{w}_{k-1}$  which is a zero-mean multivariate GP over the  $n_s$  space locations with covariance function expressed as,

$$\begin{aligned} \mathbf{w}_{k-1} &\sim \mathcal{GP}(\mathbf{0}, \mathbf{K}_s \otimes w_{k-1}) \\ w_{k-1} &= \int_0^{\Delta t_k} \mathbf{A}_{k-1} \mathbf{L} \mathbf{Q}_c \mathbf{L}^\top \mathbf{A}_{k-1}^\top d\tau. \end{aligned} \quad (11)$$

Here  $\mathbf{K}_s$  is the  $n_s \times n_s$  covariance matrix of the spatial kernel  $k(s, s')$  at  $n_s$  locations, and spectral density matrix  $\mathbf{Q}_c$  is decided by the temporal kernel  $k(t, t')$  as a mathematical combination of kernel hyperparameters.

Once the GP is formulated as a discrete-time LTI system, both the estimation of posterior predictive distribution in eqn. 5 and the hyperparameter NLML in eqn. 6 can be achieved recursively using a Kalman filter and Rauch-Tung-Striebel (RTS) smoother (Särkkä and Svensson, 2023), enabling linear time complexity in forward model runs (Aitio et al., 2023).

## 2.2 Gaussian processes for equivalent circuit models

As shown in Fig. 1, a simple ECM is used for modelling the battery dynamics in this work. This approach is similar to the method we used in Aitio et al. Aitio et al. (2023) but simplified. The corresponding mathematical formulation is given as

$$\begin{aligned} V_{\text{term}} &= V_0(z) + R_0(z, I, \zeta) I \\ \frac{dz}{dt} &= I Q^{-1}(\zeta) \end{aligned} \quad (12)$$

where  $z$  is the SOC,  $I$  is the applied current, and  $V_0(z)$  represents the OCV-SOC curve, which is often measured at beginning of life and assumed to be fixed over life. Two timescales are included in this ECM, one is the operating timescale ( $t$ ), which is often at the seconds level. Another is the life-long aging timescale ( $\zeta$ ), which can vary from days to months depending on usage. The variables  $I$ ,  $z$ ,  $V_{\text{term}}$  are all functions of  $t$ , unless written in their discrete-time versions that are demarcated with subscripts (e.g.  $z_i$ ). For clarity the time-dependence of the continuous-time variables is assumed, rather than written out in every equation. For simplicity, we use a vector to denote operating conditions,

$$\mathbf{s} = [z, I]^\top. \quad (13)$$

The inverse capacity term  $Q^{-1}$  is modeled as a GP over  $\zeta$ , while the resistance term  $R_0$  is modeled as a GP over  $\mathbf{s}$  and  $\zeta$ ,

$$\begin{aligned} Q^{-1}(\zeta) &\sim \mathcal{GP}(m(\zeta), k(\zeta, \zeta')) \\ R_0(\mathbf{s}, \zeta) &\sim \mathcal{GP}(m(\mathbf{s}, \zeta), k((\mathbf{s}, \zeta), (\mathbf{s}', \zeta'))). \end{aligned} \quad (14)$$

Given the nonzero nature of impedance and capacity, instead of directly modelling  $R_0$  and  $Q$ , we chose to model them each as affine transformations of a zero-mean GP, which is equivalent to setting a nonzero prior mean for impedance and capacity Aitio et al. (2023). Specifically, Eqns. 14 are written as,

$$\begin{aligned} Q^{-1}(\zeta) &= q_0(1 + q(\zeta)) \\ R_0(\mathbf{s}, \zeta) &= r_0(1 + r(\mathbf{s}, \zeta)) \\ q(\zeta) &\sim \mathcal{GP}(0, k(\zeta, \zeta')) \\ r(\mathbf{s}, \zeta) &\sim \mathcal{GP}(0, k((\mathbf{s}, \zeta), (\mathbf{s}', \zeta'))) \end{aligned} \quad (15)$$

where constants  $r_0, q_0$  reflect prior assumptions for the values of  $R_0, Q^{-1}$ , respectively. In practice, these can be set to the corresponding beginning-of-life (BoL) values. As a Gaussian distribution remains Gaussian under arbitrary affine transformation,  $R_0$  and  $Q^{-1}$  are still GPs.

The operating-condition dependency on  $\mathbf{s}$  and the life-long aging dependency on  $\zeta$  are modelled with different kernels, since we expect that degradation is irreversible, whereas a more general smooth function describes operating-condition dependency,

$$k((\mathbf{s}, \zeta), (\mathbf{s}', \zeta')) = k_{\text{Matern32}}(\mathbf{s}, \mathbf{s}') k_{\text{WV}}(\zeta, \zeta') \quad (16)$$

where  $k_{\text{WV}}$  and  $k_{\text{Mat}}$  represent a Wiener velocity (WV) kernel and a Matern ( $\nu = 3/2$ ) kernel, respectively, so

$$\begin{aligned} k_{\text{WV}}(\zeta, \zeta') &= \sigma_\zeta^2 \left( \frac{\min^3(\zeta, \zeta')}{3} + |\zeta - \zeta'| \frac{\min^2(\zeta, \zeta')}{2} \right) \\ k_{\text{Mat}}(\mathbf{s}, \mathbf{s}') &= \sigma_s^2 (1 + \sqrt{3}d) \exp(-\sqrt{3}d) \\ d^2 &= |\mathbf{s} - \mathbf{s}'|^\top \begin{bmatrix} l_z^{-2} & 0 \\ 0 & l_I^{-2} \end{bmatrix} |\mathbf{s} - \mathbf{s}'|. \end{aligned} \quad (17)$$

While stationary kernels eventually converge back to the mean when extrapolated, the WV kernel is a non-stationary kernel that is more suitable for extrapolating aging trends into the future.

As shown in Fig. 2, the battery operating dynamics, described by the ECM, and aging dynamics, described by the GPs, are evaluated at two different timescales. While the ECM state ( $z$ ) changes over seconds during cycling ( $t$ ), the GPs representing  $Q^{-1}$  and  $R_0$  may change more slowly, over weeks or months, as a function of cell-aging timescale  $\zeta$ . In subsequent sections we will use discrete-time rather than continuous-time dynamics, with the indexes  $i$  and  $j$  denoting the discrete-time variables associated with  $t$  and  $\zeta$ , respectively, with the faster discrete time step size defined as  $\Delta t_i$  and the slower step size as  $\Delta \zeta_j$ .

The discrete-time state propagation for the ECM is a simple Coulomb counter that can be expressed as

$$z_i = z_{i-1} - Q^{-1} I_i \Delta t_i. \quad (18)$$

The discrete-time propagation for the inverse capacity and resistance parameters, which are GPs, can be written as

$$\begin{aligned} \mathbf{x}_{Q^{-1}, j} &= \exp(\Delta \zeta_j \mathbf{F}_{\text{WV}}) \mathbf{x}_{Q^{-1}, j-1} + w_{j-1} \\ \mathbf{x}_{R_0, j} &= \exp(\Delta \zeta_j \mathbf{I}_{n_s} \otimes \mathbf{F}_{\text{WV}}) \mathbf{x}_{R_0, j-1} + \mathbf{w}_{j-1}, \end{aligned} \quad (19)$$

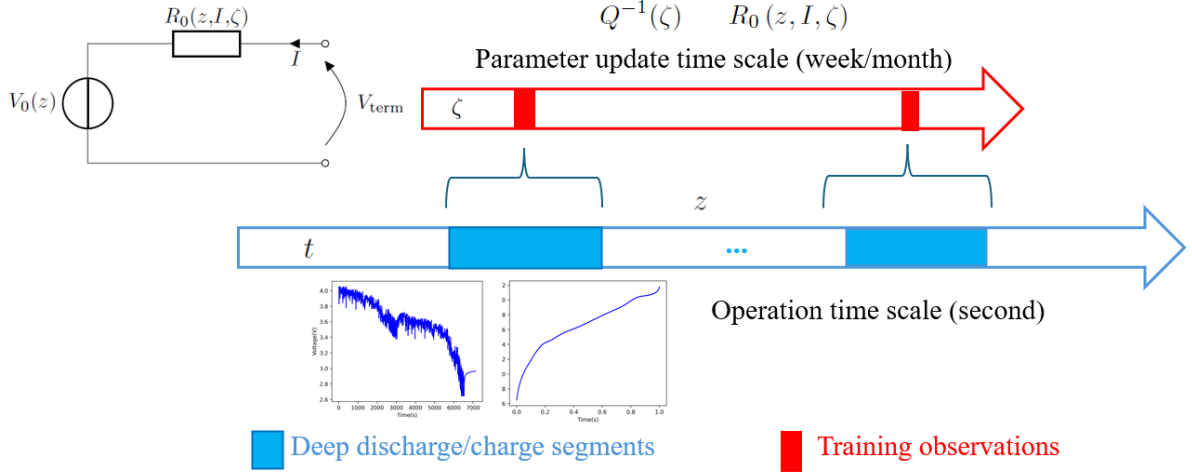


Fig. 2. Modelling the separation of timescales with battery operating dynamics that change quickly (as a function of  $t$ ) vs. aging dynamics that change slowly (as a function of  $\zeta$ )

where, for the WV kernel,  $\mathbf{F}_{\text{WV}} = \Delta\zeta_j \begin{bmatrix} 0 & 1 \\ 0 & 0 \end{bmatrix}$  represents the discrete-time interval on the lifelong aging scale. Because of the operating condition dependency of  $R_0$ , Kronecker products are used to describe the corresponding discretisation in  $\mathbf{I}_{n_s} \otimes \mathbf{F}_{\text{WV}}$  and  $\mathbf{w}_{j-1}$ . In this work,  $n_s = n_z n_I$ . Specifically, the 0 to 1 SOC range is evenly divided into  $n_z$  discrete SOC levels, while the applied current range (in absolute scale) is evenly divided into  $n_I$  discrete current levels. The process noise terms  $w_{j-1}$  and  $\mathbf{w}_{j-1}$  can be calculated following Eqn. 11, where  $Q_c$  for the WV kernel is  $\sigma_\zeta^2$ .

### 2.3 Joint estimation of battery states and GPs

The state covariance initialisation and process noise matrix of the joint system and GP subsystem are summarized as follows:

$$\mathbf{P}_{\text{joint},0} = \begin{bmatrix} \mathbf{P}_{z,0} & 0 \\ 0 & \mathbf{P}_{\text{GP},0} \end{bmatrix}, \mathbf{P}_{\text{GP},0} = \begin{bmatrix} \mathbf{P}_{Q^{-1},0} & 0 \\ 0 & \mathbf{P}_{R_0,0} \end{bmatrix}$$

$$\mathbf{W}_{\text{joint}} = \begin{bmatrix} \mathbf{W}_z & 0 \\ 0 & \mathbf{W}_{\text{GP}} \end{bmatrix}, \mathbf{W}_{\text{GP}} = \begin{bmatrix} \mathbf{W}_{Q^{-1}} & 0 \\ 0 & \mathbf{W}_{R_0} \end{bmatrix} \quad (20)$$

where

$$\mathbf{P}_{R_0,0} = \mathbf{K}_{\text{Mat}} \otimes \mathbf{P}_{\zeta_0, \text{WV}}, \quad \mathbf{P}_{Q^{-1},0} = \mathbf{P}_{\zeta_0, \text{WV}}$$

$$\mathbf{W}_{R_0} = \mathbf{K}_{\text{Mat}} \otimes \mathbf{W}_{\text{WV}}, \quad \mathbf{W}_{Q^{-1}} = \mathbf{W}_{\text{WV}}. \quad (21)$$

In these equations,  $\zeta_0$  represents the initial aging time step and  $\mathbf{K}_{\text{Mat}}$  is the covariance matrix of the Matern kernel at  $n_z$  discrete SOC levels. For the selected WV kernel, the initial covariance and noise matrix are

$$\mathbf{P}_{\zeta_0, \text{WV}} = \sigma_z^2 \begin{bmatrix} \frac{1}{3}\zeta_0^3 & \frac{1}{2}\zeta_0^2 \\ \frac{1}{2}\zeta_0^2 & \zeta_0 \end{bmatrix}, \mathbf{W}_{\text{WV}} = \sigma_z^2 \begin{bmatrix} \frac{1}{3}\Delta\zeta^3 & \frac{1}{2}\Delta\zeta^2 \\ \frac{1}{2}\Delta\zeta^2 & \Delta\zeta \end{bmatrix}. \quad (22)$$

In literature, several works (Hu et al., 2012; Wassiliadis et al., 2018) use a dual estimation framework to propagate these two subsystems separately, with the estimated SOC ( $z$ ) as the ‘observation’ for parameter updates. One major drawback of this approach is the parameter estimation performance depends strongly on the SOC accuracy. Also, by

decoupling states from parameters, any cross-correlations between the two are lost and this may lead to poor estimation accuracy (Plett, 2015). For example, the uncertainty information from the SOC estimation, which is important for parameter updates, is discarded. As an alternative, other works (Liu et al., 2020; Yu et al., 2017) adopt a joint estimation framework with a single timescale to update both states and parameters. This may suffer from poor numerical conditioning, though, due to the vastly different timescales of the state and parameter dynamics (seconds versus months).

To address these issues, we adopted our previously proposed co-estimation framework (Aitio and Howey, 2021). Within charge or discharge segments, the GP states (i.e. parameters) and the ECM state are propagated jointly. Between segments, however, only the GP states are propagated and the ECM state is reinitialized at the beginning of every segment. In this way, the GPs and ECM each share the same observations (eqn. 12), but their propagation is at different timescales.

Within a segment, the overall joint state vector for both ECM and GPs is given by

$$\mathbf{x}_{\text{joint},i} = \begin{bmatrix} z_i \\ \mathbf{x}_{Q^{-1},i} \\ \mathbf{x}_{R_0,i} \end{bmatrix}. \quad (23)$$

Between segments, the GP subsystem is linear and the GP state vector is given by

$$\mathbf{x}_{\text{GP},j} = \begin{bmatrix} \mathbf{x}_{Q^{-1},j} \\ \mathbf{x}_{R_0,j} \end{bmatrix}. \quad (24)$$

Note that within a segment the joint system is nonlinear because Eqn. 12 is nonlinear in SOC ( $z$ ) due to the  $V_0(z)$  and  $R_0(z)$  functions. For simplicity, we write the nonlinear joint system dynamics as

$$\mathbf{x}_{\text{joint},i} = g(\mathbf{x}_{\text{joint},i-1}, I_{i-1}, \mathbf{W}_{\text{joint},i-1})$$

$$V_i = h(\mathbf{x}_{\text{joint},i}, I_{i-1}, v_i). \quad (25)$$

An extended Kalman filter is used to solve the system dynamics with local linearisation via Jacobian matrices

$$\mathbf{G}_i = \frac{dg}{d\mathbf{x}_{\text{joint},i}}, \quad \mathbf{H}_i = \frac{dh}{d\mathbf{x}_{\text{joint},i}}. \quad (26)$$

The full co-estimation framework is given in Algorithm 1. Because  $R_0$  is modelled with a GP, its predictive variance needs to be included when calculating the noise covariance of output (the  $I_i^2 \Sigma_{R_0, i}$  term in  $\mathbf{S}_i$ ). Detailed derivations can be found in Appendix A and B.

**Algorithm 1** Co-estimation of battery state and GPs using extended Kalman filter. The NLML ( $\Phi$ ) is calculated recursively on every terminal voltage measurement.

---

```

1: Initialisation at  $\zeta = \zeta_0$ 
2:  $\mathbf{x}_{\text{GP}}^+ = \mathbf{x}_{\text{GP},0}, \mathbf{P}_{\text{GP}}^+ = \mathbf{P}_{\text{GP},0}$ 
3:  $\Phi = 0$ 
4: for  $\text{seg}_j \in \text{segments}$  do
5:   GP propagation
6:    $\mathbf{x}_{\text{GP},j}^- = \exp(\mathbf{F}\Delta\zeta_j)\mathbf{x}_{\text{GP},j-1}^+$ 
7:    $\mathbf{P}_{\text{GP},j}^- = \exp(\mathbf{F}\Delta\zeta_j)\mathbf{P}_{\text{GP}}^+ \exp(\mathbf{F}\Delta\zeta_j)^\top + \mathbf{W}_{\text{GP}}(\Delta\zeta_j)$ 
8:   Initialisation at start of  $j$ th segment
9:    $\mathbf{x}_{\text{joint}}^+ = \mathbf{x}_{\text{joint},0} = [z_0, \mathbf{x}_{\text{GP},j}^-]^\top$ 
10:   $\mathbf{P}_{\text{joint}}^+ = \mathbf{P}_{\text{joint},0} = \begin{bmatrix} \mathbf{P}_{z,0} & 0 \\ 0 & \mathbf{P}_{\text{GP},j}^- \end{bmatrix}$ 
11:  for  $V_i \in \text{seg}_j$  do
12:    Joint states propagation
13:     $\mathbf{x}_{\text{joint},i}^- = g(\mathbf{x}_{\text{joint},i-1}^+, I_{i-1}, \mathbf{W}_{\text{joint},i-1})$ 
14:     $\mathbf{P}_{\text{joint},i}^- = \mathbf{G}_{i-1} \mathbf{P}_{\text{joint},i-1}^+ \mathbf{G}_{i-1}^\top + \mathbf{W}_{\text{joint},i-1}$ 
15:    Joint states update
16:     $\mathbf{e}_i = V_i - h(\mathbf{x}_{\text{joint},i}^-, I_{i-1}, v_i)$ 
17:     $\mathbf{S}_i = \mathbf{H}_i \mathbf{P}_{\text{joint},i}^- \mathbf{H}_i^\top + I_i^2 \Sigma_{R_0, i} + \sigma_v^2$ 
18:     $\mathbf{L}_i = \mathbf{P}_{\text{joint},i}^- \mathbf{H}_i^\top \mathbf{S}_i^{-1}$ 
19:     $\mathbf{x}_{\text{joint},i}^+ = \mathbf{x}_{\text{joint},i}^- + \mathbf{L}_i \mathbf{e}_i$ 
20:     $\mathbf{P}_{\text{joint},i}^+ = (\mathbf{I} - \mathbf{L}_i \mathbf{H}_i)^\top \mathbf{P}_{\text{joint},i}^- (\mathbf{I} - \mathbf{L}_i \mathbf{H}_i) + \mathbf{L}_i \mathbf{e}_i \mathbf{L}_i^\top$ 
21:     $\Phi = \Phi + \frac{1}{2} \mathbf{e}_i^\top \mathbf{S}_i^{-1} \mathbf{e}_i + \frac{1}{2} \log |2\pi \mathbf{S}_i|$ 
22:  end for
23: end for

```

---

### 3. DATA PREPROCESSING AND MODEL SETUP

#### 3.1 Data description

*Cell A* Cell A is a nickel-manganese-cobalt vs. graphite Li-ion battery from an open test dataset (Thelen et al., 2023). It is a commercial 502030 cell with nominal capacity 250mAh and operating voltage from 3.0 to 4.2V. The true initial capacity was measured as around 280mAh and the beginning-of-life DC resistance around 130m $\Omega$ . This battery was aged with repeated charge/discharge cycles and checked through a weekly reference performance test (RPT). Cycling aging was conducted with a constant 1.825C charging C-rate and a constant 0.5C discharging C-rate. The depth of discharge (DoD) was 100% and the environmental temperature was kept at 30°C. The RPT consisted of low rate (0.2C) constant-current constant-voltage (CC-CV) charging and constant-current discharging, yielding ground truth discharge capacity measurements and an up-to-date pseudo OCV-SOC curve. The cell number is G37C2 in the original dataset.

*Cell B* Cell B is a nickel-cobalt-aluminium oxide vs. graphite-silicon battery from another open dataset (Jöst et al., 2021), with cell ID 015. It is a commercial 18650 cell with nominal capacity 3400mAh and BoL DC resistance

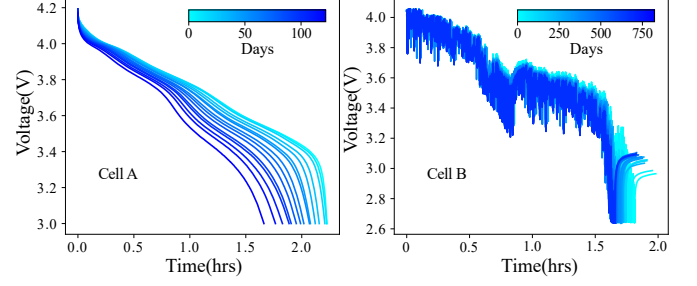


Fig. 3. All extracted discharge segments, cells A and B

around 25m $\Omega$ . This battery was charged with a CC-CV regime and discharged using a scaled drive cycle profile from 0–9.7A (absolute value). Cycle aging was conducted at 25°C between 10% and 90% SOC. Regular RPTs were taken every 30 cycles, at 0.1C.

#### 3.2 Extracting discharge segments from cycling data

The sampling frequency for cycling was 0.2 Hz and 1 Hz for cells A and B, respectively. The corresponding full cycling datasets (over all of life) are 1,840,632 and 41,346,756 rows of current and voltage measurements, respectively. Using the entire cycle life data to optimize GP hyperparameters requires substantial computational effort. However, it is reasonable to assume that the aging between two adjacent cycles is small, and therefore we only selected a small number of cycling segments from which to train the model, with relatively large between-segment distances  $\Delta\zeta_j$ .

In this work, 15 and 18 discharge segments were extracted and used for fitting, for cells A and B respectively, spread evenly across battery life (in the sense of total cycle number), reducing the data volume to 21,881 and 12,0801 rows, respectively. In practice, the time interval between segments can be adjusted according to usage and test conditions. The first 10 segments were used to train the model (i.e. to optimize the kernel hyperparameters for the GPs), but only the RPT data at BoL was used to calibrate the OCV-SOC relationship. The extracted discharge segments for cells A and B are shown in Fig. 3. The aging effect can be clearly seen from the shrinkage of discharge curves on the time axis.

#### 3.3 Modelling assumptions

Considering the computational cost and data range, we set the operating condition discretization for cell A to  $n_z = 25$  and  $n_I = 1$ , and for cell B to  $n_z = 25$  and  $n_I = 5$ .

## 4. RESULTS AND DISCUSSION

#### 4.1 Health estimation and prediction

Fig. 4 and Fig. 5 show projections of the GP estimates of discharge capacity  $Q$  and impedance  $R_0$  over battery lifetime for cells A and B, respectively. The train-test split is shown by the vertical black line. For cell A, the discharge current is constant, thus  $R_0$  is only plotted against SOC. For cell B, with dynamic discharging profile,  $R_0$  is plotted against both SOC and applied current.

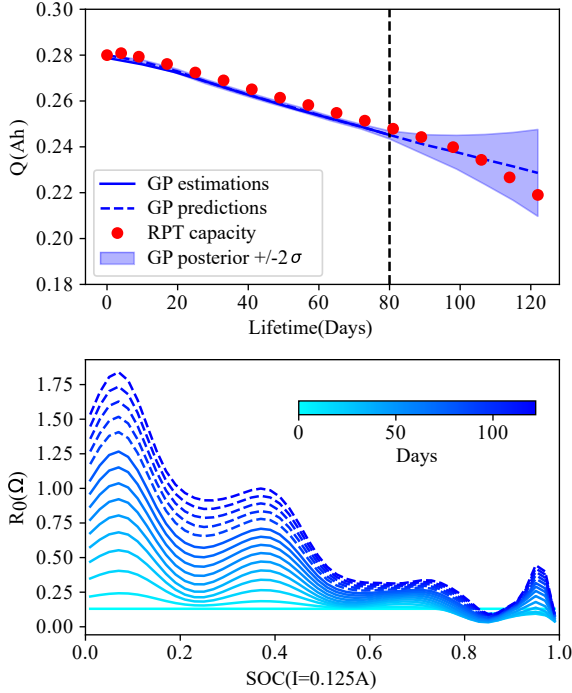


Fig. 4. Cell A projections of GP posteriors for  $Q$  and  $R_0$ . Ground truth RPTs are only used for capacity validation (red dots). RMSE and MAPE for capacity estimates are 0.0026 Ah and 0.86%, and for predictions are 0.0038 Ah and 1.53%

It is clear that the GP captures the aging trend for capacity fade well based only on cycling data without RPTs. As the non-stationary WV kernel is used for modelling the time dependency of  $Q^{-1}(\zeta)$ , the GP extrapolation maintains the last known aging trend from the training stage. This linear extrapolation fits well for cell B, while it appears slightly worse for cell A where the ground truth aging speed accelerates in later life. The uncertainty for estimates is shown by the shaded area that grows larger when extrapolating further into the future.

For the estimation results of  $R_0$ , a clear upwards shift can be found for cell A during aging, indicating a systematic increase of battery resistance over all SOC levels. For cell B,  $R_0$  changes in a more complex way, with both increasing and decreasing trends observed against different SOC levels. The scale of  $R_0$  dependency on applied current is much smaller than the SOC dependency. Thus, we mainly discuss the SOC dependency in this work, and more details about the applied current dependency can be found in Appendix C.

All estimations are shown in solid lines, extrapolations are shown as dot lines. The blue gradient colors denote the corresponding aging times. The extrapolation for  $R_0$  also maintains the increasing trend of training stage. To keep the figure simple, the uncertainty for  $R_0$  estimations are included in Fig. 7.

In order to ensure smoothness in the estimated  $R_0$  functions that are displayed, the discretization of SOC was further increased to 100 evenly spaced locations. The trained model was then rerun in forward mode, with the previously

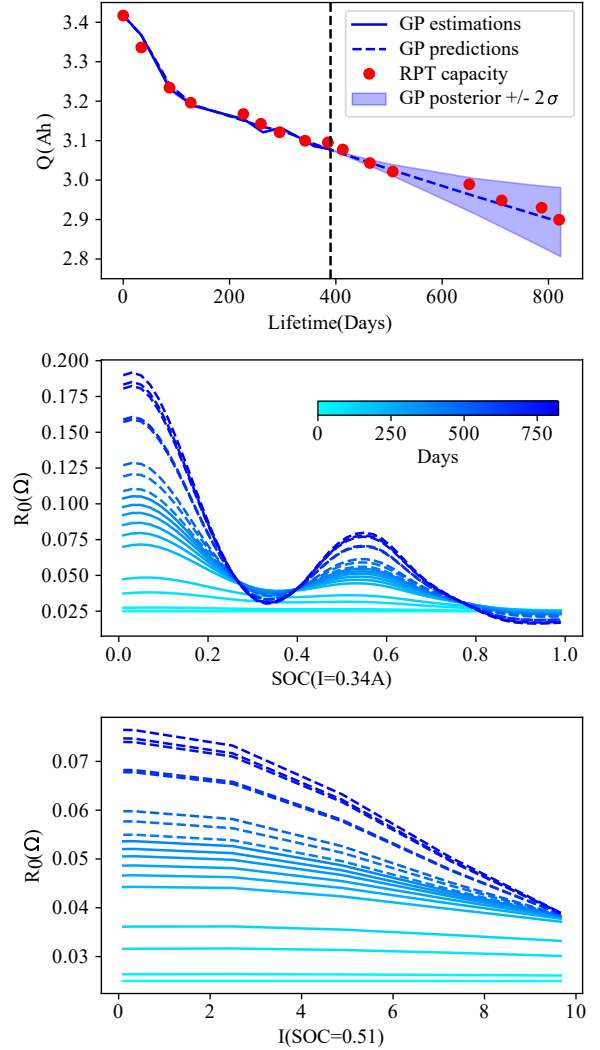


Fig. 5. Cell B projections of GP posteriors for  $Q$  and  $R_0$ . Ground truth RPTs are only used as capacity validations (red dots). RMSE and MAPE for capacity estimates are 0.0122 Ah and 0.31%, and for predictions are 0.009 Ah and 0.27%

learned GP hyperparameters, but using the extended SOC discretization.

#### 4.2 Dependence of $R_0$ on SOC

Considering the results of the previous section, there are two abnormal features to note in the evolution of  $R_0(z, \zeta)$ . First, the increasing scale of  $R_0$  is much larger than expected. Given that the BoL DC resistance calculated from a pulse test is around  $0.13 \Omega$  and  $0.025 \Omega$  for cells A and B respectively, the increase in  $R_0$  by nearly five times at low SOC level as the cell ages seems unrealistic. Second, there is a wave-like curve shape and a corresponding uneven increase of resistance against SOC. This SOC dependency is also observed by others (Waag et al., 2013; Schönleber et al., 2017). Fig. 7 shows impedance increases at different SOC levels. In the training set, the increase at high SOC ( $> 0.9$ ) is almost negligible for both cells. However, at low SOC ( $< 0.1$ ), the increase of  $R_0$  is nearly  $0.88 \Omega$  and  $0.07 \Omega$  for cell A and B respectively.

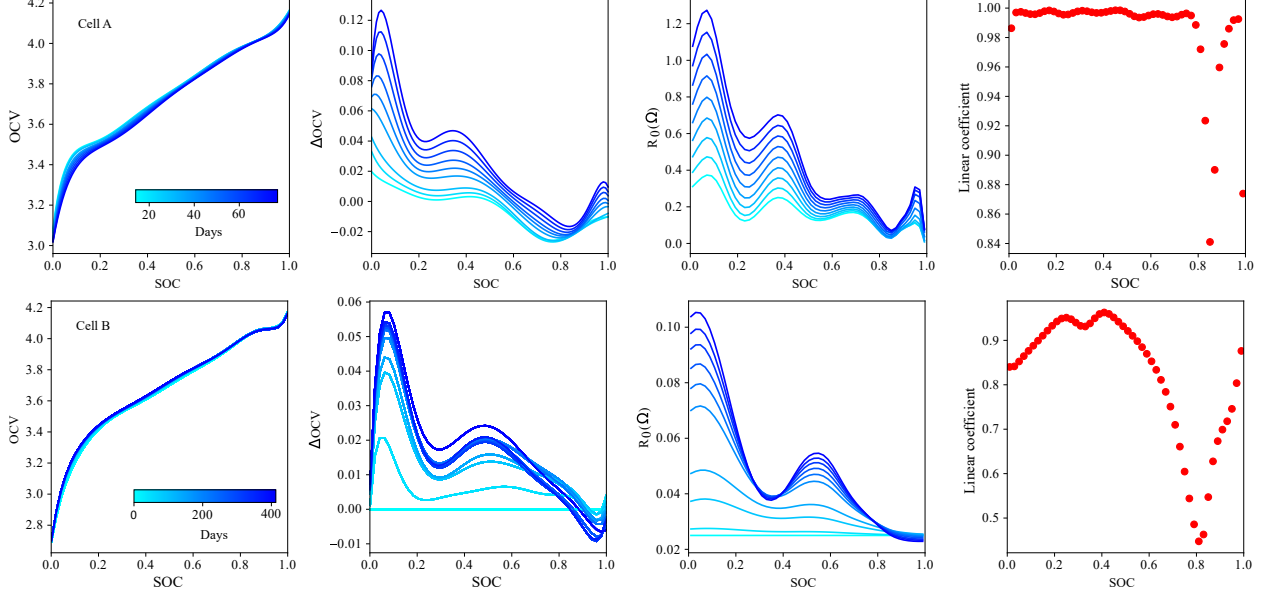


Fig. 6. Comparison between ground-truth OCV-SOC and the estimated  $R_0$  function for cell A and B

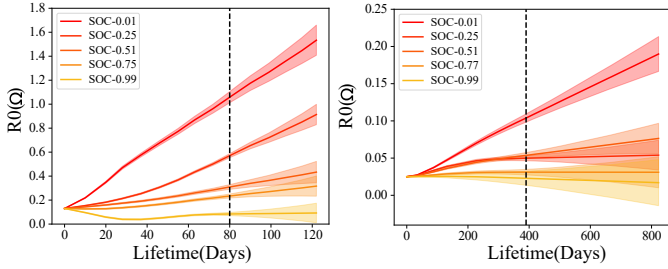


Fig. 7. The GP estimation of impedance increase on different SOC levels

We propose that these unexpected behaviours are not caused by ‘true’ changes in the underlying resistance, but instead hypothesize that a significant reason for increases in the estimated  $R_0(z, \zeta)$  is shape changes in the battery OCV-SOC curve as it ages. Specifically, the battery dynamics in Eqn. 12 assume that the OCV-SOC functional relationship is kept the same across the entire life, and only scaled by  $Q$ . A more realistic formulation could be expressed as

$$V_{\text{term}} = V_0(z, \zeta) + \hat{R}_0(z, \zeta)I, \quad (27)$$

where the OCV-SOC relationship  $V_0(z, \zeta)$  is itself a function of both SOC ( $z$ ) and aging lifetime ( $\zeta$ ). In this case,  $\hat{R}_0$  is the ‘pure’ impedance term (unaffected by OCV). By further separating the OCV term into a fixed part  $\bar{V}_0(z, \zeta_0)$  (representing BoL OCV-SOC), and an age-sensitive variable part  $\Delta V_0(z, \zeta)$ , one can rewrite this equation as

$$V_{\text{term}} = \bar{V}_0(z, \zeta_0) + \Delta V_0(z, \zeta) + \hat{R}_0(z, \zeta)I$$

$$V_{\text{term}} = \bar{V}_0(z) + I \underbrace{\left[ \frac{\Delta V_0(z, \zeta)}{I} + \hat{R}_0(z, \zeta) \right]}_{R_0(z, \zeta)}. \quad (28)$$

It is now clear that, rather than obtaining the pure resistance  $\hat{R}_0$ , the learnt function  $R_0(z, \zeta)$  is influenced both by changes in the resistance and changes in the OCV-SOC functional form as the battery ages.

Thanks to the regular RPT data, we are able to validate this hypothesis using ground-truth OCV-SOC changes. Fig. 6 compares the learnt  $R_0(z, \zeta)$  functions and ground-truth OCV-SOC curves. The applied current was 0.125 A and 0.34 A for cells A and B, respectively. Here,  $\Delta\text{OCV}$  represents the difference between ‘up-to-date’ OCVs (i.e., incorporating changes as the cell ages) and BoL OCVs across all SOC levels. A strong consistency can be observed in the changing trends of  $R_0$  and  $\Delta\text{OCV}$ . This can be quantified using a Pearson linear correlation coefficient—specifically, for each discrete SOC value, the linear coefficient between  $R_0$  and  $\Delta\text{OCV}$  as a function of age was calculated. For cell A, a linear coefficient of more than 0.8 is observed over all SOC levels, decreasing slightly around 0.8 SOC. Similarly, for cell B, a coefficient of more than 0.7 is seen for most SOC levels, decreasing around 0.8 SOC.

One remaining issue concerns the (un)identifiability of  $\Delta V_0(z, \zeta)$  and  $\hat{R}_0(z, \zeta)$ . Given the additive nature of these, it is impossible to distinguish them individually from terminal voltage measurements. However, the differences of their influences on terminal voltage can be compared. If one assumes, for example, a 50% increase in resistance compared to BoL DC resistance, this would result in overpotential changes of 8 mV and 4 mV for cells A and B at 0.5C and 0.1C, respectively. However, the average changes in the OCV-SOC function over life are 30 mV and 20 mV, respectively—on the order of ten times higher.

#### 4.3 Differential voltage analysis

Capacity decrease and impedance increase reflect battery SOH changes at the full cell level, but are insufficient to elucidate different degradation modes. One commonly used quantitative method for the latter is differential voltage analysis ( $dV/dQ$  vs. discharge Ah). The  $dV/dQ$  curve is obtained by differentiating discharge voltage with respect to cumulative discharge Ampere-hours. The peaks on the  $dV/dQ$  curve can be assigned to electrode material phase transitions. The peak shifts and the chang-

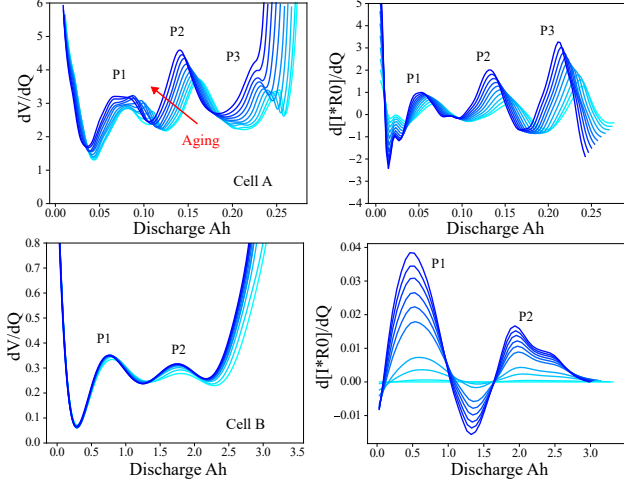


Fig. 8. The comparison between RPT  $dV/dQ$  and estimated  $d[IR_0]/dQ$

ing between-peak distances are used to indicate different degradation modes, i.e. lost lithium inventory LLI, and loss of active material in the negative and positive electrodes,  $LAM_n$  and  $LAM_p$  (Dubarry and Anseán, 2022). One major limitation of the  $dV/dQ$  method is the requirement for a low C-rate ( $< C/20$ ) deep (dis)charge, which is generally unavailable except in a carefully controlled lab environment. In our case, because of experiment limits, the RPT C-rates for cells A and B were higher, at  $C/5$  and  $C/10$ , respectively.

Given the observed close similarity between  $\Delta OCV(z, \zeta)$  and  $R_0(z, \zeta)$  as discussed in the previous section, a natural extension is to compare the  $dV/dQ$  information from the RPTs with the learnt  $d[IR_0]/dQ$  vs. discharge curve. As shown in Fig. 8, if one multiplies the SOC with the learnt capacity  $Q(\zeta)$ , one can derive a corresponding discharge Ampere-hour estimate and thus observe similar peak shifts to differential voltage functions.

Due to the lack of half cell test data, we are not able to attribute each  $dV/dQ$  peak to a corresponding electrode, and thus cannot directly calculate LLI,  $LAM_n$  and  $LAM_p$ . However, quantitative analysis of shifts in peaks ( $P_1$ ,  $P_2$  and  $P_3$ ) were calculated and are shown in Fig. 9. For both cells, the estimated peak shifts of  $d[IR_0]/dQ$  cover similar ranges and have similar trends compared to the ground-truth peak shifts of  $dV/dQ$ , with some differences. Specifically, there is a divergence between estimates and ground truth of  $P_1$  shifts for cell A. The ground truth  $P_1$  splits into two peaks during aging, and this is not captured in the  $d[IR_0]/dQ$  estimates.

## 5. CONCLUSIONS

We have proposed an aging-aware battery ECM incorporating GPs to describe the dependency of circuit-model parameters on SOC and lifetime. A state-space formulation was used to transform the GPs into time-stepping models enabling solution in linear time complexity with a Kalman filter and RTS smoother. This also enables co-estimation of both parameters and states in a unified framework. Compared to parameter random walks or deterministic

models, using GPs to model parameter evolution has several advantages:

- The state-space formulation of a GP maintains gradient information from the states whilst random walk or empirical models do not.
- Incorporating the SOC and aging-time dependency of parameters via GP kernels makes ECM parameter estimates more stable over battery life, i.e. gives smoother interpolation and more reasonable extrapolation compared to random walk or deterministic models.
- A GP prior helps to mitigate numerical ill-conditioning as it has a regularisation effect when parameters are not easily identifiable (e.g. due to measurement noise or extrapolation to unseen conditions).

We found that estimates of capacity  $Q$  exhibited good consistency compared with independent ground-truth measurements from RPTs, whereas estimates of the resistance function  $R_0$  showed a close relationship with shape changes in the OCV-SOC curve as a battery ages. A major part of the learnt  $R_0(z, \zeta)$  function comes from OCV changes,  $\Delta V_0(z, \zeta)$ . High linear coefficients ( $> 0.8$ ) were observed between  $R_0(z, \zeta)$  and  $\Delta V_0(z, \zeta)$  over a wide range of SOCs. By using the estimates of both  $Q(\zeta)$  and  $R_0(z, \zeta)$ , we further calculated  $d[IR_0]/dQ$  as an approximation to a differential voltage  $dV/dQ$  function. The estimated peak shifts in  $d[IR_0]/dQ$  were found to show similar behaviours compared with ground-truth peak shifts in  $dV/dQ$ .

This work highlights both a challenge, to ensure that shape changes to the OCV curve do not distort battery SOH estimates, and an opportunity—to estimate degradation modes (lost lithium inventory, lost electrode material) directly from operational data. Further tests are required on other cell form factors, duty cycles (e.g. shallow cycling), chemistries, and cell sizes to explore the generalisation of these results.

## Appendix A. GAUSSIAN PROCESS WITH INPUT UNCERTAINTY

In the joint system dynamics (eqn. 25),  $R_0$  needs to be evaluated at every time step. The SOC at step  $i$  is itself a Gaussian distribution expressed as

$$z_i \sim \mathcal{N}(z_i^-, \mathbf{P}_{z_i}^-). \quad (\text{A.1})$$

This means that  $R_0$  is a GP with input uncertainty from  $z_i$ . To incorporate this, the predictive distribution in eqn. 5 needs to be marginalised (averaged) over all  $z_i$ ,

$$p(R_0) = \int p(R_0 | z_i) p(z_i) dz_i. \quad (\text{A.2})$$

This integral is usually intractable but can be approximated using Taylor expansions (Girard et al., 2002). A first-order expansion can be written as

$$\begin{aligned} m_{R_0} &= K_{Z, z_i}^\top [K_Z + \sigma_{\text{GP}}^2 I]^{-1} z_i \\ \Sigma_{R_0} &= K_{z_i, z_i} - K_{Z, z_i}^\top [K_Z + \sigma_{\text{GP}}^2 I]^{-1} K_{Z, z_i} \\ &\quad + \left. \frac{\partial R_0}{\partial z} \right|_{z_i}^\top \mathbf{P}_{z_i}^- \left. \frac{\partial R_0}{\partial z} \right|_{z_i}. \end{aligned} \quad (\text{A.3})$$

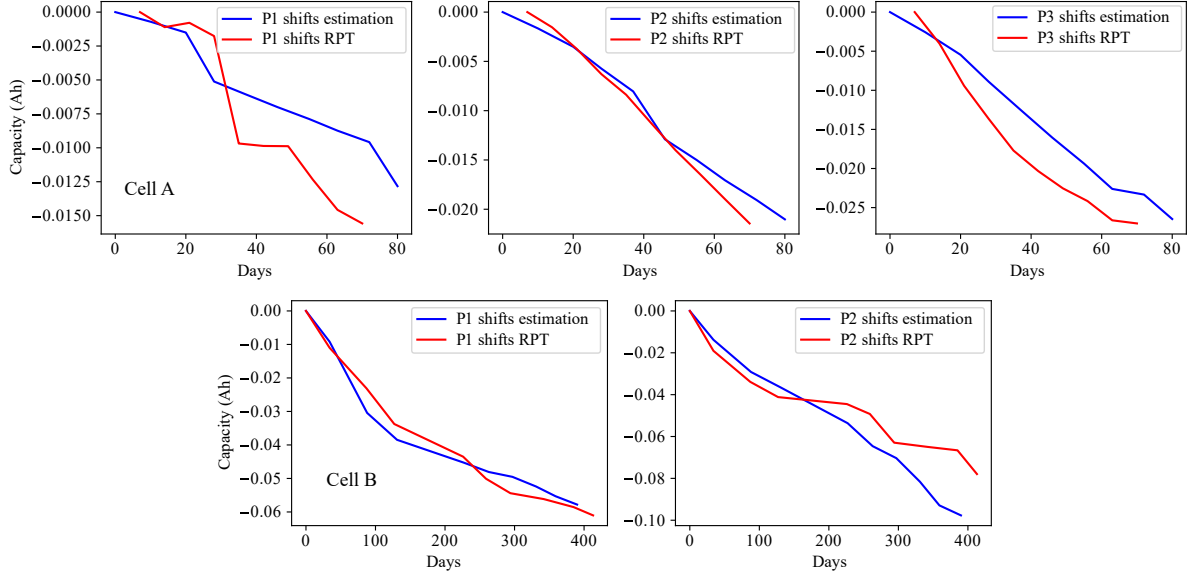


Fig. 9. Comparison of peak(P1,P2,P3) shifts for  $dV/dQ$  from RPTs and  $d[IR_0]/dQ$  estimations.

## Appendix B. PREDICTIVE VARIANCES FOR TERMINAL VOLTAGE

In the extended Kalman filter used for the joint GP-ECM system, an extra variance term  $I_i^2 \Sigma_{R_{0,i}}$  is included in the calculation of the innovation sequence  $\mathbf{S}_i$ . This corresponds to the contribution of the  $R_0$  uncertainty when calculating the predictive distribution of terminal voltage  $V_i$ :

$$\begin{aligned} V_i &= V_0(z_i) + I_i R_{0,i} + \nu_i, \quad \nu_i \sim N(0, \sigma_\nu^2) \\ E[V_i] &= V_0(z_i) + I_i m_{R_{0,i}} \\ \text{cov}(V_i) &= E[(V_i - E[V_i])(V_i - E[V_i])^\top] \\ \text{cov}(V_i) &= I_i^2 \Sigma_{R_{0,i}} + \sigma_\nu^2. \end{aligned} \quad (\text{B.1})$$

## Appendix C. IMPEDANCE DEPENDENCY ON APPLIED CURRENT

Fig. C.1 gives a full set of resistance estimates at several SOCs and currents, for cell A.

## REFERENCES

- Aitio, A. and Howey, D.A. (2021). Predicting battery end of life from solar off-grid system field data using machine learning. *Joule*, 5(12), 3204–3220.
- Aitio, A., Jöst, D., Sauer, D.U., and Howey, D. (2023). Learning battery model parameter dynamics from data with recursive gaussian process regression. *Journal of Dynamic Systems, Measurement, and Control*, 1–13.
- Bericibar, M., Gandiaga, I., Villarreal, I., Omar, N., Van Mierlo, J., and Van den Bossche, P. (2016). Critical review of state of health estimation methods of li-ion batteries for real applications. *Renewable and Sustainable Energy Reviews*, 56, 572–587.
- Cohen, L. (1998). The generalization of the wiener-khinchin theorem. In *Proceedings of the 1998 IEEE International Conference on Acoustics, Speech and Signal Processing, ICASSP'98 (Cat. No. 98CH36181)*, volume 3, 1577–1580. IEEE.
- Dubarry, M. and Anseán, D. (2022). Best practices for incremental capacity analysis. *Frontiers in Energy Research*, 10, 1023555.
- Dubarry, M., Truchot, C., and Liaw, B.Y. (2012). Synthesize battery degradation modes via a diagnostic and prognostic model. *Journal of power sources*, 219, 204–216.
- Feng, X., Weng, C., He, X., Han, X., Lu, L., Ren, D., and Ouyang, M. (2019). Online state-of-health estimation for li-ion battery using partial charging segment based on support vector machine. *IEEE Transactions on Vehicular Technology*, 68(9), 8583–8592.
- Fu, Y., Xu, J., Shi, M., and Mei, X. (2021). A fast impedance calculation-based battery state-of-health estimation method. *IEEE Transactions on Industrial Electronics*, 69(7), 7019–7028.
- Gao, Y., Liu, K., Zhu, C., Zhang, X., and Zhang, D. (2021). Co-estimation of state-of-charge and state-of-health for lithium-ion batteries using an enhanced electrochemical model. *IEEE Transactions on Industrial Electronics*, 69(3), 2684–2696.
- Girard, A., Rasmussen, C., Candela, J.Q., and Murray-Smith, R. (2002). Gaussian process priors with uncertain inputs application to multiple-step ahead time series forecasting. *Advances in neural information processing systems*, 15.
- Greenbank, S. and Howey, D. (2021). Automated feature extraction and selection for data-driven models of rapid battery capacity fade and end of life. *IEEE Transactions on Industrial Informatics*, 18(5), 2965–2973.
- Hu, C., Youn, B.D., and Chung, J. (2012). A multiscale framework with extended kalman filter for lithium-ion battery soc and capacity estimation. *Applied Energy*, 92, 694–704.
- Hua, Y., Liu, X., Zhou, S., Huang, Y., Ling, H., and Yang, S. (2021). Toward sustainable reuse of retired lithium-ion batteries from electric vehicles. *Resources, Conservation and Recycling*, 168, 105249.

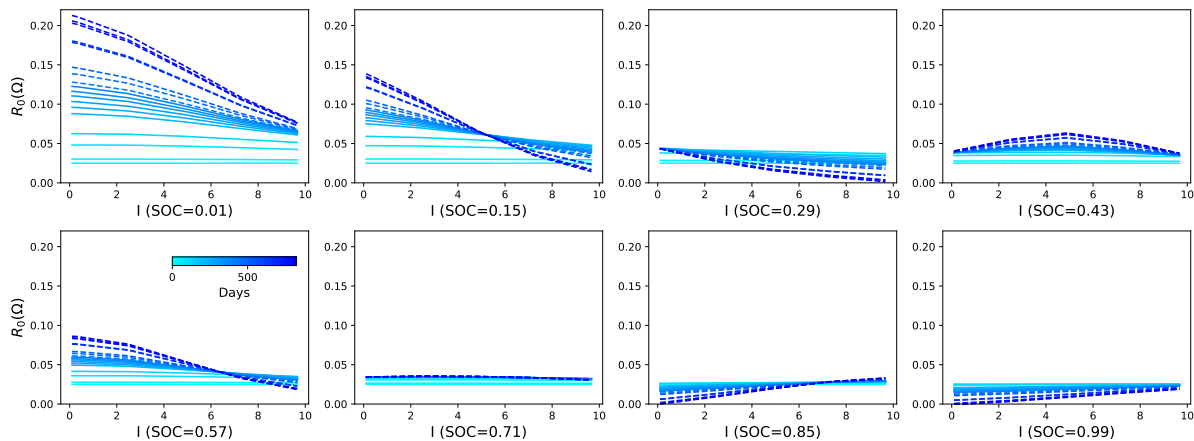


Fig. C.1. Dependence of resistance on applied current at several SOCs, for cell A

- Jöst, D., Blömeke, A., Sauer, D.U., and Ringbeck, F. (2021). Timeseries data of a drive cycle aging test of 28 high energy nca/c+ si round cells of type 18650. Technical report, Institut für Stromrichtertechnik und Elektrische Antriebe.
- Li, T., Zhou, Z., Thelen, A., Howey, D.A., and Hu, C. (2024). Predicting battery lifetime under varying usage conditions from early aging data. *Cell Reports Physical Science*, 5(4).
- Li, W., Sengupta, N., Dechent, P., Howey, D., Annaswamy, A., and Sauer, D.U. (2021). Online capacity estimation of lithium-ion batteries with deep long short-term memory networks. *Journal of power sources*, 482, 228863.
- Li, Y., Liu, K., Foley, A.M., Zülke, A., Bercibar, M., Nanini-Maury, E., Van Mierlo, J., and Hoster, H.E. (2019). Data-driven health estimation and lifetime prediction of lithium-ion batteries: A review. *Renewable and sustainable energy reviews*, 113, 109254.
- Li, Y., Zou, C., Bercibar, M., Nanini-Maury, E., Chan, J.C.W., Van den Bossche, P., Van Mierlo, J., and Omar, N. (2018). Random forest regression for online capacity estimation of lithium-ion batteries. *Applied energy*, 232, 197–210.
- Liu, B., Tang, X., and Gao, F. (2020). Joint estimation of battery state-of-charge and state-of-health based on a simplified pseudo-two-dimensional model. *Electrochimica Acta*, 344, 136098.
- Locorotondo, E., Cultrera, V., Pugi, L., Berzi, L., Pierini, M., and Lutzemberger, G. (2021). Development of a battery real-time state of health diagnosis based on fast impedance measurements. *Journal of Energy Storage*, 38, 102566.
- Lu, D., Trimboli, M.S., Fan, G., Zhang, R., and Plett, G.L. (2021). Implementation of a physics-based model for half-cell open-circuit potential and full-cell open-circuit voltage estimates: part i. processing half-cell data. *Journal of The Electrochemical Society*, 168(7), 070532.
- Miguel, E., Plett, G.L., Trimboli, M.S., Oca, L., Iraola, U., and Bekaert, E. (2021). Review of computational parameter estimation methods for electrochemical models. *Journal of Energy Storage*, 44, 103388.
- Plett, G.L. (2004). Extended kalman filtering for battery management systems of lipb-based hev battery packs: Part 3. state and parameter estimation. *Journal of Power sources*, 134(2), 277–292.
- Plett, G.L. (2015). *Battery management systems, Volume II: Equivalent-circuit methods*. Artech House.
- Pozzato, G., Allam, A., Pulvirenti, L., Negoita, G.A., Paxton, W.A., and Onori, S. (2023). Analysis and key findings from real-world electric vehicle field data. *Joule*, 7(9), 2035–2053.
- Richardson, R.R., Birkl, C.R., Osborne, M.A., and Howey, D.A. (2018). Gaussian process regression for in situ capacity estimation of lithium-ion batteries. *IEEE Transactions on Industrial Informatics*, 15(1), 127–138.
- Sarkka, S., Solin, A., and Hartikainen, J. (2013). Spatiotemporal learning via infinite-dimensional bayesian filtering and smoothing: A look at gaussian process regression through kalman filtering. *IEEE Signal Processing Magazine*, 30(4), 51–61.
- Särkkä, S. and Svensson, L. (2023). *Bayesian filtering and smoothing*, volume 17. Cambridge university press.
- Schönleber, M., Uhlmann, C., Braun, P., Weber, A., and Ivers-Tiffée, E. (2017). A consistent derivation of the impedance of a lithium-ion battery electrode and its dependency on the state-of-charge. *Electrochimica Acta*, 243, 250–259.
- Severson, K.A., Attia, P.M., Jin, N., Perkins, N., Jiang, B., Yang, Z., Chen, M.H., Aykol, M., Herring, P.K., Fragedakis, D., et al. (2019). Data-driven prediction of battery cycle life before capacity degradation. *Nature Energy*, 4(5), 383–391.
- Shahjalal, M., Roy, P.K., Shams, T., Fly, A., Chowdhury, J.I., Ahmed, M.R., and Liu, K. (2022). A review on second-life of li-ion batteries: Prospects, challenges, and issues. *Energy*, 241, 122881.
- Solin, A. et al. (2016). *Stochastic differential equation methods for spatio-temporal Gaussian process regression*. Ph.D. thesis, Aalto University.
- Sulzer, V., Mohtat, P., Aitio, A., Lee, S., Yeh, Y.T., Steinbacher, F., Khan, M.U., Lee, J.W., Siegel, J.B., Stefanopoulou, A.G., et al. (2021). The challenge and opportunity of battery lifetime prediction from field data. *Joule*, 5(8), 1934–1955.
- Thelen, A., Li, T., Liu, J., Tischer, C., and Hu, C. (2023). Isu-ilcc battery aging dataset. <https://doi.org/10.25380/iastate.22582234.v2>. doi:10.25380/iastate.22582234.v2.

- Tsiropoulos, I., Tarvydas, D., Lebedeva, N., et al. (2018). *Li-ion batteries for mobility and stationary storage applications*. Publications Office of the European Union.
- Waag, W., Käbitz, S., and Sauer, D.U. (2013). Experimental investigation of the lithium-ion battery impedance characteristic at various conditions and aging states and its influence on the application. *Applied energy*, 102, 885–897.
- Wang, Y., Tian, J., Sun, Z., Wang, L., Xu, R., Li, M., and Chen, Z. (2020). A comprehensive review of battery modeling and state estimation approaches for advanced battery management systems. *Renewable and Sustainable Energy Reviews*, 131, 110015.
- Wassiliadis, N., Adermann, J., Frericks, A., Pak, M., Reiter, C., Lohmann, B., and Lienkamp, M. (2018). Revisiting the dual extended kalman filter for battery state-of-charge and state-of-health estimation: A use-case life cycle analysis. *Journal of Energy Storage*, 19, 73–87.
- Wei, J., Dong, G., and Chen, Z. (2017). Remaining useful life prediction and state of health diagnosis for lithium-ion batteries using particle filter and support vector regression. *IEEE Transactions on Industrial Electronics*, 65(7), 5634–5643.
- Williams, C.K. and Rasmussen, C.E. (2006). *Gaussian processes for machine learning*. MIT press Cambridge, MA.
- Yu, Q., Xiong, R., Lin, C., Shen, W., and Deng, J. (2017). Lithium-ion battery parameters and state-of-charge joint estimation based on h-infinity and unscented kalman filters. *IEEE Transactions on Vehicular Technology*, 66(10), 8693–8701.
- Zhou, Z., Ran, A., Chen, S., Zhang, X., Wei, G., Li, B., Kang, F., Zhou, X., and Sun, H. (2020). A fast screening framework for second-life batteries based on an improved bisecting k-means algorithm combined with fast pulse test. *Journal of Energy Storage*, 31, 101739.